PHYSICAL REVIEW E **102**, 062705 (2020)

# Dynamics of defects around anisotropic particles in nematic liquid crystals under shear

Humberto Híjar [*]
*La Salle University Mexico, Benjamín Franklin 45, 06410 Mexico City, Mexico*

(Received 1 September 2020; accepted 7 December 2020; published 28 December 2020)

Nematic multiparticle collision dynamics is used to simulate disclination ring defects around spherocylinders suspended in a liquid crystal. A solvent-solute interaction potential is integrated over a short-time scale by an auxiliary molecular dynamics procedure that updates the translational and angular coordinates of the spherocylinders. For suspended particles with length in the range ∼(60, 160) nm and a fixed aspect ratio, this method is able to simulate static defects reported previously in the literature. It also simulates orientation fluctuations of the elongated colloids that exhibit a broad distribution and a slow relaxation rate. Finally, a nematic host driven from equilibrium by shear flow is simulated, and the consequent dynamic behavior of the colloid-defect pair is studied. Defects under shear present significant structural transformations from chairlike disclination rings to extended defects that cover most of the cylindrical surface of the colloid. This effect results from the hydrodynamic torque on the nematic field caused by the distorted flow around the spherocylinder, and it is present for small Reynolds and Ericksen numbers of order unity.

DOI: 10.1103/PhysRevE.102.062705

## I. INTRODUCTION

Suspensions of colloids and nanoparticles in liquid crystals are enormously interesting because of fundamental and technological reasons [1]. The inclusion of micron-sized and nanosized particles in a nematic medium creates topological defects in the director field, with the average molecular alignment direction denoted by the unit vector $\hat{\mathbf{n}}$. Defects promote long-range distortions and anisotropic forces that sustain self-assembly and entanglement of colloidal chains or crystals that could have applications for, e.g., photonic crystals and optical cavities [2], and composite materials with new classes of responses to external stimuli [3].

Defects are generated when the constraints imposed by the shape and anchoring conditions of the guest particles disagree with orientations in the bulk. Then, discontinuities in $\hat{\mathbf{n}}$ are created that are accompanied by a pronounced local reduction of order [4]. Strong distortions at the core relax by aligning molecular orientations along the biaxial direction, and the defect core itself can be identified as a region of strong biaxiality [5,6].

Spherical colloids with homeotropic anchoring conditions, for which solvent molecules prefer to be perpendicular to the intruder surfaces, exhibit three types of defects in a nematic in thermodynamic equilibrium: (i) the dipole configuration, characterized by the formation of a hyperbolic hedgehog; (ii) the quadrupolar configuration, where the colloid is surrounded by a disclination ring (Saturn-ring); and (iii) the surface-ring configuration, where the core of the disclination ring sits directly at the surface of the colloid [7]. The occurrence of these different defects is governed by the colloidal size and the anchoring strength [7–9]. Anisotropic colloids create more complex defects and assembly mechanisms in the nematic host. This has been demonstrated through the analysis of a variety of structures including polygonal platelets [10], as well as star, bullet, fractal, and peanut-shaped colloids [11–14].

Colloids with simpler but still nontrivial geometries, e.g., spherocylinders, ellipsoids, and bars, have been investigated with the aim of exploring the torques and equilibrium orientations that anisotropic particles encounter in a uniform nematic, the defect structures that they produce, and the resulting liquid-crystal-mediated interactions [4,15–24]. For homeotropic conditions, the equilibrium state of elongated particles with respect to the far director field, $\hat{\mathbf{n}}_0$, has been observed to depend on the aspect ratio, the length scale, the anchoring strength, and the shape of the two particles' ends [4,18,20,22]. It is expected that infinitely long cylinders equilibrate either parallel or perpendicular to $\hat{\mathbf{n}}_0$ depending on the ratio of the particle's radius to the extrapolation length of the solvent [15]. Micron-sized rods supplied with strong homeotropic conditions create dipolar defects that are stable when the long symmetry axis of the rod is parallel or slightly tilted with respect to $\hat{\mathbf{n}}_0$, whereas quadrupolar defects appear and are stable over a large angular range around perpendicular alignment [17]. Changes from microscopic to mesoscopic and nanoscopic scales induce the appearance of additional metastable defects around rodlike particles that are also highly dependent on the spatial orientation. For mesoscopic rods and parallel alignment, three structures—top-ring, chairlike, and mid-ring-0—have been identified using a model of free-energy minimization [22]. For perpendicular alignment, the same model yields also three different defects, referred to as chairlike, boatlike, and mid-ring-90. However, for nanosized rods only one type of defect is found for perpendicular alignment consisting of a ring perpendicular to $\hat{\mathbf{n}}_0$, whereas for the parallel configuration the only defect is an extended ring or "axially symmetric coat" that covers the entire lateral surface of the rod [22]. Indeed, these latter structures turned out to be very similar to those that were found earlier in studies

---

[*] humberto.hijar@lasalle.mx

of meso- and nanometric spherocylinders in nematic liquid crystals modeled through a partial differential equation for the evolution of the tensor order parameter, $\mathbb{Q}$ [4,18]. Thus, defects around elongated particles with lengths ∼40–1000 nm could be considered well explored for solvents in equilibrium. In contrast, the influence of nonequilibrium conditions on the structural properties of these topological defects has been much less investigated.

Flow is a nonequilibrium agent that perturbs topological defects. When colloids are placed in a flowing nematic, the stream causes reorientation of $\hat{\mathbf{n}}$ and a consequential distortion of the associated defects. Flow past a colloid with a Saturn ring induces a displacement of the disclination along the stream direction and leads to a quadrupole-dipole transformation as the ring shrinks in the wake [25–27]. Simulations including solution of the equations for $\mathbb{Q}$ under an adaptive mesh refinement [28], fluid particle dynamics [29], and nematic multiparticle collision dynamics (N-MPCD) [30] have been able to simulate this phenomenon. Downstream displacement and deformation of quadrupole defects have been also simulated for colloids in a nematic under Poiseuille flow [31,32]. Defects and flow forces experienced by spherical colloids in nematic microfluidic channels have also been investigated [33,34]. Noticeably, the effects of flow on defects around anisotropic particles in liquid crystals have been rarely, if ever, studied. In this paper, N-MPCD simulations are conducted to analyze the dynamics of defects around mesoscopic elongated particles driven by a nematic solvent under nonequilibrium flow conditions. More precisely, a nematic performing tumbling motion by the action of a uniform shear flow is considered to host a mesoscopic spherocylinder that enforces strong homeotropic conditions. The dynamics of the solvent is simulated under the coarse-grained rules of N-MPCD that allow nematohydrodynamic effects to be incorporated while solid-fluid interactions are taken into account through molecular dynamics (MD) of the translational and rotational motion of the guest particle. First, it is shown that defects simulated by MD-N-MPCD for static spherocylindrical colloids of length ≃(60, 160 nm) have the expected structural and energetic properties previously reported for systems of similar form, size, and aspect ratio [4,16,18,22]. Afterwards, it is found that the orientation of simulated spherocylinders moving freely in a quiescent nematic fluctuates around configurations of low elastic energy over broad distributions which resemble those measured experimentally for ensembles of anisotropic colloids of similar size and aspect ratio but different shape [14,17,35]. Nonequilibrium simulations are presented subsequently. Flow is restricted to small Reynolds numbers and Ericksen numbers of order unity. It is shown that shear promotes substantial changes of the elastic energy and significant structural changes of the topological defects. These effects are due to the relative rotation of the solvent and the colloid that induces inhomogeneous hydrodynamic torques on $\hat{\mathbf{n}}$.

## II. SIMULATION METHOD

The algorithm is particle-based. Solvent particles, hereafter referred to as pseudonematogens, are point particles of mass $m$ carrying a unit orientation vector, $\hat{\mathbf{u}}_i$, where $i = 1, 2, \ldots, N$, and $N$ is their total number. Their positions and velocities are denoted as $\mathbf{r}_i$ and $\mathbf{v}_i$, respectively. A spherocylindrical colloid consisting of a cylinder of length $L$ and hemispheric caps of radius $\sigma$ is immersed in the solvent. Its center-of-mass position and velocity are $\mathbf{R}$ and $\mathbf{V}$, respectively. $\mathbf{R}$, $\mathbf{V}$, $\mathbf{r}_i$, and $\mathbf{v}_i$ are defined with respect to a laboratory reference frame spanned by the orthonormal base $\{\hat{\mathbf{e}}_1, \hat{\mathbf{e}}_2, \hat{\mathbf{e}}_3\}$. A moving coordinate system attached to the colloid is spanned by the set $\{\hat{\mathbf{e}}'_1, \hat{\mathbf{e}}'_2, \hat{\mathbf{e}}'_3\}$, where $\hat{\mathbf{e}}'_3$ indicates the direction of the long symmetry axis. The principal moments of inertia of the colloid in the moving system are $J_3$ and $J_1 = J_2$. Particles move in a box of sizes $L_1$, $L_2$, and $L_3$. The evolution of the system occurs over two separated timescales: a short timescale that takes into account direct solvent-colloid interactions and a mesoscopic timescale where hydrodynamic modes of the solvent relax toward equilibrium. To simulate the effects occurring in both scales, two time intervals, $\Delta t_{\rm MD}$ and $\Delta t \gg \Delta t_{\rm MD}$, are introduced. Over the former, the equations of motion are integrated under a MD scheme, whereas over the latter, collective momentum and orientation exchanges are simulated. Both processes are described as follows.

### A. Molecular dynamics integration of spherocylinder motion

Pseudonematogens interact with the colloid through the repulsive potential [36]

$$\Phi(\mathbf{r}_i - \mathbf{R}) = \begin{cases} 4\epsilon\Big[\big(\frac{\sigma}{\ell_i}\big)^{12p} - \big(\frac{\sigma}{\ell_i}\big)^{6p} + \frac{1}{4}\Big] & \text{if } \ell_i \leqslant 2^{1/6p}\sigma, \\ 0 & \text{otherwise,} \end{cases} \tag{1}$$

where $\ell_i$ is the shortest distance from $\mathbf{r}_i$ to the segment line of length $L$ running from cap to cap along $\hat{\mathbf{e}}'_3$, $\epsilon$ is the potential strength (depth of the uncut unshifted Lennard-Jones potential), and $p$ is a positive integer that controls the stiffness of the potential. Variables $\mathbf{r}_i$, $\mathbf{v}_i$, $\mathbf{R}$, and $\mathbf{V}$ are updated over $\Delta t_{\rm MD}$ using the velocity-Verlet integrator [37]. In this process, forces on solvent and solute particles are $\mathbf{f}_i = -\partial\Phi/\partial\mathbf{r}_i$ and $\mathbf{F} = -\sum_{i=1}^{N}\mathbf{f}_i$, respectively.

Spherocylinder rotation is treated by the method of Omelyan [38], in which $\hat{\mathbf{e}}'_1$, $\hat{\mathbf{e}}'_2$, and $\hat{\mathbf{e}}'_3$ are used as orientational variables that are integrated within a velocity-Verlet scheme. More precisely, let $\mathbb{A}$ be the rotation matrix that relates the orientation of the spherocylinder with the laboratory fixed coordinate system, i.e., $A_{\alpha\beta} = \hat{\mathbf{e}}'_\alpha \cdot \hat{\mathbf{e}}_\beta$, where $\alpha, \beta = 1, 2, 3$. In addition, define the principal components of the angular velocity of the spherocylinder, $\mathbf{\Omega} = \Omega_1\hat{\mathbf{e}}'_1 + \Omega_2\hat{\mathbf{e}}'_2 + \Omega_3\hat{\mathbf{e}}'_3$, and the matrix $\mathbb{W}$ with components $W_{\alpha\beta} = \epsilon_{\alpha\beta\gamma}\Omega_\gamma$, where $\epsilon_{\alpha\beta\gamma}$ is the Levi-Civita symbol. Then, the evolution of $\mathbb{A}$ can be approximated as follows:

$$\mathbb{A}(t + \Delta t_{\rm MD}) = \mathbb{A}(t) + \dot{\mathbb{A}}(t)\Delta t_{\rm MD} + \tfrac{1}{2}\ddot{\mathbb{A}}(t)(\Delta t_{\rm MD})^2, \tag{2}$$

where $\dot{\mathbb{A}}$ can be evaluated using the relation $\dot{\mathbb{A}} = \mathbb{W} \cdot \mathbb{A}$, and $\ddot{\mathbb{A}} = \dot{\mathbb{W}} \cdot \mathbb{A} + \mathbb{W} \cdot \mathbb{W} \cdot \mathbb{A}$ can be evaluated using the Euler equation

$$\dot{\Omega}_1(t) = \tfrac{1}{J_1}[\kappa_1(t) + (J_2 - J_3)\Omega_2(t)\Omega_3(t)], \tag{3}$$

and those obtained from cyclic permutations for $\dot{\Omega}_2(t)$ and $\dot{\Omega}_3(t)$. In Eq. (3) and those corresponding to $\dot{\Omega}_2(t)$ and $\dot{\Omega}_3(t)$, $\kappa_1$, $\kappa_2$, and $\kappa_3$ are the components of the torque exerted on the colloid with respect to its center of mass due to the interactions with the pseudonematogens, $\boldsymbol{\kappa} = \kappa_1 \hat{\mathbf{e}}'_1 + \kappa_2 \hat{\mathbf{e}}'_2 + \kappa_3 \hat{\mathbf{e}}'_3$. They can be calculated from the vector $\mathbf{k} = -\sum_{i=1}^{N} (\mathbf{r}_i - \mathbf{R}) \times \mathbf{f}_i$, and the transformation $\boldsymbol{\kappa} = \mathbb{A} \cdot \mathbf{k}$.

Equation (2) is supplemented with the rule for updating $\mathbb{W}$, i.e., $\boldsymbol{\Omega}$,

$$\boldsymbol{\Omega}(t + \Delta t_{\mathrm{MD}}) = \mathbb{J}^{-1} \cdot \mathbb{A}(t + \Delta t_{\mathrm{MD}}) \cdot \mathbf{l}(t + \Delta t_{\mathrm{MD}}), \tag{4}$$

where the angular momentum of the solute in the laboratory frame, $\mathbf{l}$, is updated in a velocity-Verlet fashion, namely

$$\mathbf{l}(t + \Delta t_{\mathrm{MD}}) = \mathbf{l}(t) + \tfrac{1}{2}[\mathbf{k}(t) + \mathbf{k}(t + \Delta t_{\mathrm{MD}})]\Delta t_{\mathrm{MD}}. \tag{5}$$

### B. Anchoring conditions

Homeotropic anchoring on the surface of the colloid is simulated by reorienting pseudonematogens along the normal direction if $\ell_i \leqslant 2^{1/6} p\sigma$. Accordingly, the colloid's surface is accompanied by a varying number of perpendicular pseudonematogens that interact periodically with those in the bulk through the process that will be described in Sec. II C. This causes reorientation of the nematic close to the colloid, and it permits the formation of topological defects [30]. This mechanism is reinforced by adding virtual pseudonematogens on the surface of the spherocylinder. Virtual particles are initialized at random positions satisfying $\ell_i = 2^{1/6} p\sigma$. Their positions relative to the frame $\{\hat{\mathbf{e}}'_1, \hat{\mathbf{e}}'_2, \hat{\mathbf{e}}'_3\}$ are fixed. They are kept normal to the spherocylinder's surface at all times, and they are considered to be massless so that they do not modify the equations of motion. However, they are allowed to contribute to the local value of $\mathbb{Q}$ and thus to influence the orientation field close to the colloid.

### C. Nematic multiparticle collision dynamics

The dynamics at the mesoscopic scale is simulated using the N-MPCD approach as proposed in Ref. [39]. At time intervals of size $\Delta t$, the simulation box is mentally divided in cubic cells of volume $a^3$, hereafter referred to as collision cells. For every collision cell, the center-of-mass position $\mathbf{r}^{\mathrm{c}}$, velocity $\mathbf{v}^{\mathrm{c}}$, and orbital inertia tensor $\mathbb{J}^{\mathrm{c}}$ are calculated. Translation invariance of N-MPCD is obtained by shifting the grid of collision cells by a random vector with components $a_{\mathrm{rnd},1}, a_{\mathrm{rnd},2}, a_{\mathrm{rnd},3} \in (0, a]$, before particles are sorted into the cells [40].

Finite differences of $\mathbf{v}^{\mathrm{c}}$ are used to estimate the velocity gradient tensor whose symmetric and antisymmetric parts are denoted as $\mathbb{C}^{\mathrm{c}}$ and $\mathbb{D}^{\mathrm{c}}$, respectively.

The order parameter tensor at collision cell c is calculated using

$$\mathbb{Q}^{\mathrm{c}} = \frac{1}{2\mathcal{N}^{\mathrm{c}}} \sum_{j \in \mathrm{c}}^{*} (3\hat{\mathbf{u}}_j \hat{\mathbf{u}}_j - \mathbb{I}), \tag{6}$$

where $\mathbb{I}$ is the identity matrix and $\sum^{*}$ extends over solvent particles, virtual pseudonematogens attached at the surface of the spherocylinder, and possible virtual particles resulting from the presence of confining walls, as will be described in Sec. II D. Moreover, in Eq. (6), $\mathcal{N}^{\mathrm{c}}$ is the number of all these types of particles contained in the collision cell.

The order parameter $S^{\mathrm{c}}$ is defined as the largest eigenvalue of $\mathbb{Q}^{\mathrm{c}}$ [5,6,41]. The director $\hat{\mathbf{n}}^{\mathrm{c}}$ is the corresponding eigenvector. The biaxiality $P^{\mathrm{c}}$ can be calculated as the absolute value difference between the middle and largest eigenvalues of $\mathbb{Q}^{\mathrm{c}}$ [16]. Solvent particles interact with those located within the same collision cell through the mean-field potential

$$\mathcal{U}(\hat{\mathbf{u}}_i; \hat{\mathbf{n}}^{\mathrm{c}}) = -\tfrac{3}{2} U S^{\mathrm{c}} \big[(\hat{\mathbf{u}}_i \cdot \hat{\mathbf{n}}^{\mathrm{c}})^2 - \tfrac{1}{3}\big], \tag{7}$$

where $U$ is the interaction strength, a simulation specified parameter that governs the tendency of solvent particles to follow $\hat{\mathbf{n}}^{\mathrm{c}}$. New orientations $\hat{\mathbf{u}}'_i$ are sampled from a canonical distribution proportional to $\exp\{-\beta\mathcal{U}\}$, where $\beta = 1/k_{\mathrm{B}}T$, $k_{\mathrm{B}}$ is the Boltzmann constant, and $T$ is the temperature. Flow reorientation is simulated by a further transformation that yields vectors $\hat{\mathbf{u}}''_i$ taken from the Jeffery's equation for slender rods under flow,

$$\hat{\mathbf{u}}''_i = \hat{\mathbf{u}}'_i + \chi_{\mathrm{HI}}[\mathbb{C}^{\mathrm{c}} \cdot \hat{\mathbf{u}}'_i + \lambda(\mathbb{D}^{\mathrm{c}} \cdot \hat{\mathbf{u}}'_i - \mathbb{D}^{\mathrm{c}} : \hat{\mathbf{u}}'_i \hat{\mathbf{u}}'_i \hat{\mathbf{u}}'_i)]\Delta t. \tag{8}$$

In Eq. (8), $\chi_{\mathrm{HI}} \in [0, 1]$ is a control parameter that tunes the alignment relaxation time relative to $\Delta t$ [39], while $\lambda$ is related to the tumbling parameter, $\lambda'$, by [42]

$$\lambda' = \lambda \frac{15S + 48S_4 + 42}{105S}, \tag{9}$$

where $S$ and $S_4$ are the second and fourth scalar order parameters of the solvent [43]. For $\lambda' < 1$, $\hat{\mathbf{u}}_i$ tumbles, while for $\lambda' > 1$, it is stabilized by shear at the so-called Leslie-angle [44].

The Anderson thermostat [39,45] gives new velocities for solvent particles,

$$\mathbf{v}'_i = \mathbf{v}^{\mathrm{c}} + \boldsymbol{\xi}_i - \boldsymbol{\xi}^{\mathrm{c}} - [(\mathbb{J}^{\mathrm{c}})^{-1} \cdot \Delta\mathbf{L}^{\mathrm{c}}] \times (\mathbf{r}_i - \mathbf{r}^{\mathrm{c}}), \tag{10}$$

where $\boldsymbol{\xi}_i$ is a random velocity sampled from the Maxwell distribution at temperature $T$, $\boldsymbol{\xi}^{\mathrm{c}} = \sum_{j \in \mathrm{c}} \boldsymbol{\xi}_i / N^{\mathrm{c}}$, and $\Delta\mathbf{L}^{\mathrm{c}}$ is the angular momentum generated by random velocity sampling, $\Delta\mathbf{L}^{\mathrm{c}}_{\mathrm{ran}}$, and reorientation of solvent particles, $\Delta\mathbf{L}^{\mathrm{c}}_{\mathrm{ori}}$. The former reads

$$\Delta\mathbf{L}^{\mathrm{c}}_{\mathrm{ran}} = \sum_{j \in \mathrm{c}} (\mathbf{r}_j - \mathbf{r}^{\mathrm{c}}) \times (\mathbf{v}_j - \boldsymbol{\xi}_j), \tag{11}$$

whereas the latter is calculated under the assumption of overdamped reorientation as

$$\Delta\mathbf{L}^{\mathrm{c}}_{\mathrm{ori}} = \gamma_{\mathrm{R}} \sum_{j \in \mathrm{c}} \hat{\mathbf{u}}''_j \times \hat{\mathbf{u}}_j, \tag{12}$$

where $\gamma_{\mathrm{R}}$ is an heuristic viscous rotation coefficient that quantifies the transferred angular momentum from orientation back into linear momentum, i.e., backflow [39]. At this point, it is mentioned that in alternative N-MPCD techniques, backflow can be resolved directly from nematohydrodynamic theories [46,47].

### D. Boundary conditions

Throughout, periodic boundary conditions are applied along $\hat{\mathbf{e}}_1$ and $\hat{\mathbf{e}}_2$ directions. To simulate confinement between solid walls, bounce-back boundary conditions [48] are applied during MD integration at planes $x_3 = 0$ and $x_3 = L_3$. Confinement causes partially empty collision cells that are commonly treated by using virtual particles [49–51]. Here, two extra slices of width $a - a_{\mathrm{rnd},3}$ and $a_{\mathrm{rnd},3}$ are added at the bottom and top of the simulation box, respectively, and filled with virtual pseudonematogens at the same density as the solvent. Virtual particles are uniformly distributed at random positions within the extra slices. They participate in the momentum exchange events having mass $m$, and velocities sampled from a zero-average Maxwell-Boltzmann distribution at temperature $T$. Furthermore, they are conveniently used to model anchoring at the solid surface [39,47]. With this purpose, orientations of virtual particles are chosen to coincide with the preferred vector $\hat{\mathbf{e}}_3$. This imposes strong homeotropic anchoring conditions at the solid walls. Since virtual pseudonematogens are allowed to influence the orientation exchange process through Eq. (6), the bulk orientation in the vicinity of the walls is kept close to $\hat{\mathbf{e}}_3$.

Uniform shear is simulated using Lees-Edwards boundary conditions [52]. Flow is restricted to a point along $\hat{\mathbf{e}}_1$ and to increase as a function of $x_3$ with shear rate $\dot{\gamma}$. For $\dot{\gamma} = 0$, periodic boundary conditions along the three Cartesian axes are recovered.

### E. System parameters

Simulations are conducted for solvents with $U = 6.5\, k_{\mathrm{B}}T$ and $\bar{N}^{\mathrm{c}} = 20$, 25, and 30, where $\bar{N}^{\mathrm{c}}$ is the average number of pseudonematogens per cell. Using the complete set of simulation parameters specified in Appendix A, the average order parameters $S^{\mathrm{c}} = 0.697 \pm 0.006$, $0.712 \pm 0.006$, and $0.726 \pm 0.006$ are obtained, respectively, for each one of the aforementioned values of $\bar{N}^{\mathrm{c}}$. Colloids with three different sizes—$L = 6a$, $12a$, and $16a$—are simulated, all of them having the same aspect ratio, $\zeta = L/(2\sigma) = 2$. Throughout, $a = 1$, $m = 1$, and $\Delta t = 1$ are taken as units of length, mass, and time, respectively.

To visualize defects, isosurfaces of $S^{\mathrm{c}}$ and $P^{\mathrm{c}}$ are constructed. $P^{\mathrm{c}}$ vanishes far from the spherocylinder, but rings of strong biaxiality are identified in its vicinity. These can be associated with the core of the induced disclinations. As in previous cases [30,39], the size of the defect core is found to be $r^{\mathrm{c}} \simeq a$. By considering the typical value for actual nematics, $r^{\mathrm{c}} \simeq 10$ nm, $L$ can be scaled to $L \in (60\ \mathrm{nm}, 160\ \mathrm{nm})$.

Spherocylinders distort $\hat{\mathbf{n}}$ and increase the elastic free energy, $F$. For the used N-MPCD implementation, $F$ can be calculated under the one-constant approximation [39,53]

$$F = \frac{K}{2} \int d\mathbf{r}[(\mathrm{div}\, \hat{\mathbf{n}})^2 + (\mathrm{rot}\, \hat{\mathbf{n}})^2], \tag{13}$$

where $K$ is the elastic constant and $d\mathbf{r}$ is the volume element. In simulations, $F$ is estimated using finite spatial differences of $\hat{\mathbf{n}}^{\mathrm{c}}$ and a summation over the cells encompassed by the simulation box. Strictly speaking, this method cannot be used in the presence of defects because it could not deal with the implicit singularities of $\hat{\mathbf{n}}$. Then, it represents an approximation under the assumption that at the coarse-grained scale of N-MPCD, defect cores are not fully resolved and $\hat{\mathbf{n}}^{\mathrm{c}}$ presents no singularities. In addition, since $\hat{\mathbf{n}}^{\mathrm{c}}$ fluctuates due to the stochastic character of N-MPCD, $F$ has a fluctuating contribution whose average does not vanish because fluctuations are squared in the integrand of Eq. (13). Consequently, the average energy can be written as $\langle F \rangle = F^{(0)} + F^{(1)}$, where $F^{(0)}$ is the contribution of the colloid and $F^{(1)}$ is due to fluctuations. The latter is estimated from simulations where no particles are attached to the surface of the spherocylinder, and bulk particles do not reorient when they come into contact with it. In this case, spherocylinders are immersed in the nematic solvent, but no defects are created. For simplicity, in the following only $F^{(0)}$ will be reported, and the superscript (0) will be omitted from the notation.

Coefficients $K$ are estimated in Appendix B from correlation functions of the order parameter tensor. They have the magnitude expected from previous calculations in N-MPCD [39].

## III. RESULTS

### A. Defects around spherocylinders with fixed orientation

Defects around anisotropic particles in liquid crystals depend on their orientation and size [18,20,22]. Simulations are conducted to observe this effect via N-MPCD. To focus attention on the defect structures, rotation of the spherocylinders is suppressed during this stage. The colloid's orientation is specified by the angle between $\hat{\mathbf{e}}_3'$ and $\hat{\mathbf{e}}_3$: $\theta$. Spherocylinders of length $L = 6a$, $12a$, and $16a$ are confined in cubic boxes of volume $V = (32a)^3$, $(40a)^3$, and $(56a)^3$, respectively. Three orientations are considered for each $L$ value: $\theta = 0^\circ$, $30^\circ$, and $90^\circ$. Pseudonematogens are initially oriented along $\hat{\mathbf{e}}_3$. The system thermalizes while defects start to appear. They become stable after approximately 20, 200, and 500 N-MPCD collision events for $L = 6a$, $12a$, and $16a$, respectively.

For $\hat{\mathbf{e}}_3' \parallel \hat{\mathbf{e}}_3$, three types of defects are identified that depend on $L$. These are depicted in Fig. 1 as contour surfaces for $S^{\mathrm{c}} = 0.5$. Configurations in Fig. 1 are obtained from an average over $1.5 \times 10^5$ MD-N-MPCD steps taken after a thermalization stage of the same duration. Results are illustrated solely for $\bar{N}^{\mathrm{c}} = 25$, being very similar for $\bar{N}^{\mathrm{c}} = 20$ and 30.

For $L = 6a$, the defect surrounds completely the cylindrical section of the colloid, Fig. 1(a). This "coat-type" structure agrees with those found in Refs. [4,16], and it is the expected defect around elongated particles with $L \lesssim 100$ nm [22]. In Fig. 1(a), $\hat{\mathbf{n}}^{\mathrm{c}}$ shows a very slight axial asymmetry. Although this asymmetry was reported by Andrienko and co-workers [16], it disagrees with the results of Hung *et al.* [4], who observed an axially symmetric field. These discrepancies could be given by the difference in size of the particles simulated in Ref. [4], $L = 24.8$ nm, and here $L \sim 60$ nm. This could be further explored by simulating smaller colloids, i.e., $L < 6a$ and $\sigma < 1.5a$. However, such cases are not considered here since N-MPCD does not resolve properties at scales smaller than the cell size.

In the case $L = 12a$, defects adopt one of the two possible forms shown in Fig. 1(b). The first one [Fig. 1(b), left] is a ring perpendicular to $\hat{\mathbf{e}}_3$ located with equal probability at the top or bottom edge of the cylindrical part of the colloid. The second one [Fig. 1(b), right] is formed by two symmetric circular portions located at the opposite extremes of the colloid and connected by two line segments. Hereafter, these defects will be referred to as top-ring and chairlike structures, respectively, following Hashemi and Ejtehadi, who observed similar defects around cylindrical colloids with flat ends [22].

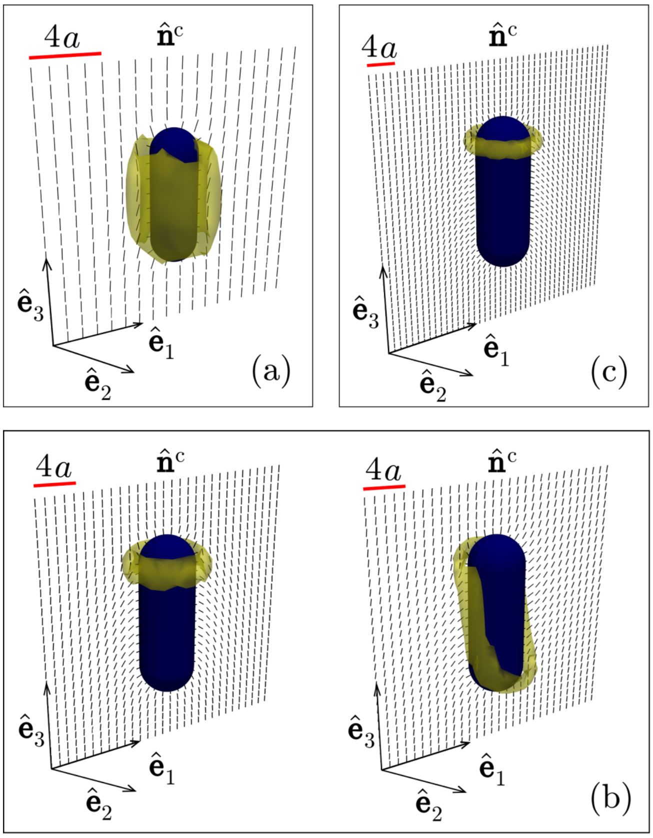

FIG. 1. Defects around spherocylindrical colloids of aspect ratio 2 in N-MPCD solvents. (a) $L = 6a$, (b) $L = 12a$, (c) $L = 16a$. The director field on the $\hat{\mathbf{e}}_1$-$\hat{\mathbf{e}}_3$ plane, $\hat{\mathbf{n}}^c$, is represented by the small line segments. In case (b) two types of defects are possible: "top-ring" (left) or "chairlike" (right).

Top-ring and chairlike defects appear stochastically from an initial unstable ring located close to the mid position of the spherocylinder. This structure either moves toward the top or bottom of the particle (top-ring) or is symmetrically stretched (chairlike). The latter has a higher energy cost. It corresponds to a local minimum state produced kinetically and is observed with a relative frequency close to 20%. For simulations lasting $3 \times 10^5$ MD-N-MPCD steps, no transitions between chairlike and top-ring defects are observed.

The only stable structure resulting after thermalization of the largest spherocylinders, $L = 16a$, is the top-ring illustrated in Fig. 1(c). The large associated energy cost prevents the occurrence of chairlike defects. Top-ring defects evolve from initial coatlike rings of high elastic energy. These unstable structures shrink close to the symmetry plane of the spherocylinder perpendicular to $\hat{\mathbf{e}}_3$. At this position rings are still unstable, and during a transient period they move up or down with equal probability, as shown in Fig. 2, where $F(t)$ is plotted and snapshots of defects at representative times are presented. The displacement of the ring toward the end of the spherocylinder resembles observations of quadrupolar defects around microrods in which, using optical tweezers, defects are forced to sit at an energetically unfavorable position from which they slide slowly to the end of the rod when tweezers are turned off [17].

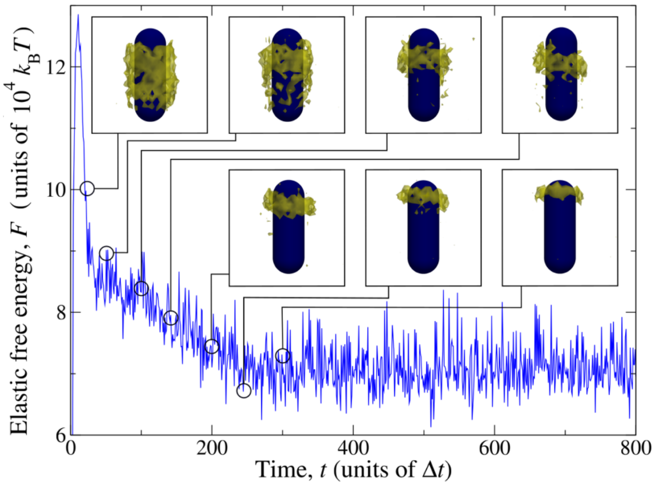

FIG. 2. Thermalization process of defects around spherocylinders with $L = 16a$. Initial extended defects of high elastic energy contract and move to the end of the colloid.

Defects for spherocylinders with $\theta = 30°$ and $90°$ are illustrated in Figs. 3(a)–3(f). Independently of $L$, only two stable structures are observed: chairlike defects for $\theta = 30°$, and Saturn rings encircling spherocylinders along their longer dimension for $\theta = 90°$. Measurements of $F$ for the combinations of parameters $\theta$ and $L$ considered up to now are presented in Table I. Perpendicular Saturn rings ($\theta = 90°$) have the lowest energies. Therefore, the spherocylinder is expected to be stable for $\hat{\mathbf{e}}_3' \perp \hat{\mathbf{e}}_3$. In addition, the relative energy difference between top-ring and chairlike defects in the case $L = 12a$ and $\bar{N}^c = 25$ is close to 8%. In cases $\bar{N}^c = 20$ and 30, the difference is found to be 13% and 10%, respectively. For defects around cylinders of flat ends, radius 160 nm, and aspect ratio 1 : 1, this difference is 3.8% [22], which should be considered for reference only due to the significant dissimilarities between the systems simulated here and in Ref. [22].

Defects in systems with $\bar{N}^c = 20$ and 30 have the same structural properties as those discussed here for $\bar{N}^c = 25$. The only difference is their associated elastic energy. For $\bar{N}^c = 20$ (30), $F$ is found to be around 7% smaller (13% larger) than in the case $\bar{N}^c = 25$. Some results for colloids with $\zeta = 1$ and 3 are given in Appendix C. No differences in the structure of defects were observed. This suggests that the defects reported here are representative of those that can be found when $\zeta$ is order unity.

### B. Orientation distribution of immersed particles

Orientations of anisotropic particles in nematic solvents exhibit broad distributions [14,17,35]. The orientation of glass rods of micrometer diameter is distributed in a large interval, 60°–90°, with respect to $\hat{\mathbf{n}}_0$ [17], though smaller tilt angles down to 40° seem to have a nonvanishing probability to occur. Glass rods having 10–20 $\mu$m length and 1.5 $\mu$m diameter, confined in cells with planar anchoring, exhibit configurations of parallel, perpendicular, and diagonal alignment to the rubbing direction. When microrods favor homeotropic anchoring on their surface, the angular distribution has a peak around a tilt angle $\theta = 60°$ [35]. Peanut-shaped particles, 3.2 $\mu$m

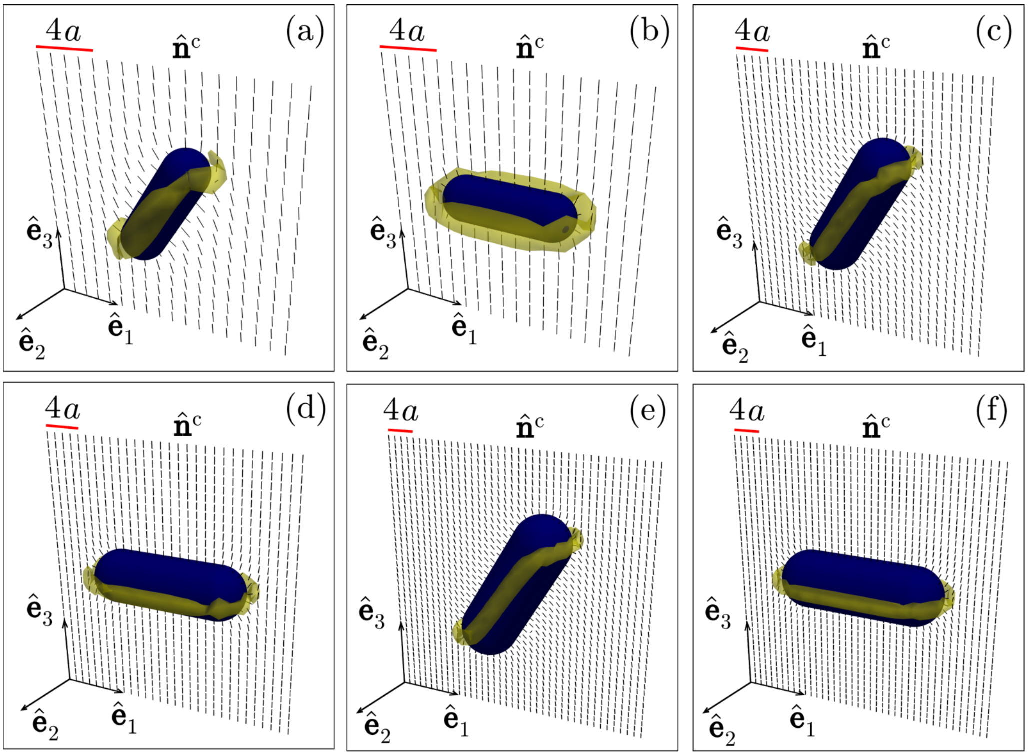

FIG. 3. Defects for colloids inclined with respect to $\hat{\mathbf{e}}_3$. (a) $L = 6a$, $\theta = 30^\circ$. (b) $L = 6a$, $\theta = 90^\circ$. (c) $L = 12a$, $\theta = 30^\circ$. (d) $L = 12a$, $\theta = 90^\circ$. (e) $L = 16a$, $\theta = 30^\circ$. (f) $L = 16a$, $\theta = 90^\circ$.

long and 1.54 $\mu$m wide, orient themselves with their long axis at all possible angles with respect to $\hat{\mathbf{n}}_0$. In this case, the probabilities for perpendicular and parallel orientations are 35% and 13%, respectively [14].

When MD-N-MPCD operates under Eqs. (2)–(4), spherocylinders are able to rotate and explore configurations with different energies. In simulations starting at $\theta = 0^\circ$, spherocylinders rotate toward states of lower energy. They seem to tend gradually to $\theta = 90^\circ$, following erratic trajectories. After some time, they fluctuate around perpendicular alignment. This is illustrated in Fig. 4(a) using time series, $\theta(t)$, from simulations of spherocylinders of size $L = 12a$, in solvents with $\bar{N}^c = 20$, 25, and 30, contained in simulation boxes with lengths $L_1 = L_2 = 56a$ and $L_3 = 40a$. Figures 4(b)–4(f) are snapshots of the system with density $\bar{N}^c = 30$, taken at the selected times indicated in the graph of Fig. 4(a).

All series in Fig. 4(a) encompass $2 \times 10^6$ MD-N-MPCD steps. By coincidence, the last state of the case, $\bar{N}^c = 30$, corresponds almost exactly to perpendicular alignment, Fig. 4(f). However, deviations from $\theta = 90^\circ$ can actually be considerably large, as in, e.g., the last states for $\bar{N}^c = 20$ and 25 in Fig. 4(a). To estimate the variability of $\theta$, simulations with initial condition $\theta(0) = 90^\circ$ are conducted also over $2 \times 10^6$ steps. Then, distributions of the inclination angle, freq($\theta$), are computed from time averages using the last $10^6$ steps of the series with initial condition $\theta(0) = 0^\circ$, and the last $1.5 \times 10^6$ steps of the series with $\theta(0) = 90^\circ$. Results for freq($\theta$) are shown in Fig. 5 for each $\bar{N}^c$ value. Though small values of $\theta$ can be observed, large tilt angles are preferred. Averages of distributions in Fig. 5 are 62.45°, 57.68°, and 59.89° for $\bar{N}^c = 20$, 25, and 30, respectively. These results are in good qualitative agreement with the aforementioned analyses of elongated particles of diverse shapes immersed in nematic phases [14,17,35]. Nonetheless, the differences in scale and morphology of the particles studied here and in Refs. [14,17,35] prevent a direct quantitative comparison of their orientation distributions.

It is important to notice that large deviations from $\theta = 90^\circ$ can be produced, although according to the results in Table I, they imply very large increments of $F$. Apart from changes in

TABLE I. Average elastic energy of defects of different sizes, $L$, inclined at angles $\theta$ with respect to the global director. Energies are given in $k_B T$ units.

| | Length | | |
|---|---|---|---|
| Inclination | $L = 6a$ | $L = 12a$ | $L = 16a$ |
| $\theta = 0^\circ$ | $16859 \pm 27$ | Top-ring: $43969 \pm 80$ Chairlike: $47805 \pm 86$ | $70868 \pm 118$ |
| $\theta = 30^\circ$ | $11806 \pm 26$ | $39697 \pm 67$ | $65494 \pm 112$ |
| $\theta = 90^\circ$ | $7638 \pm 19$ | $30180 \pm 56$ | $51272 \pm 93$ |

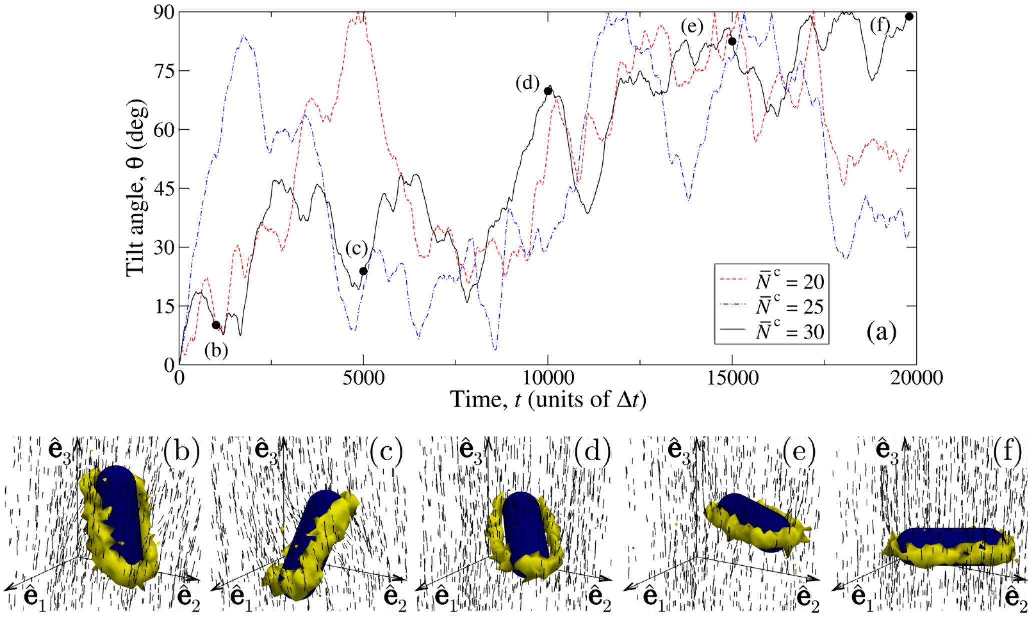

FIG. 4. Spherocylinder relaxation in a quiescent nematic. (a) Time-dependent tilt angle for densities $\bar{N}^c = 20$, 25, and 30. (b)–(f) Snapshots of the process for $\bar{N}^c = 30$; labels correspond to the points indicated along the curve in (a). Small lines indicate the instantaneous director field.

$F$, reorientation also modifies the surface anchoring energy. However, calculations of the angular distribution of pseudonematogens with respect to the normal direction on the colloidal surface indicate that relative changes of the anchoring energy are smaller than 6% in favor of $\theta = 90^\circ$. Consequently, they are not responsible for small tilt angles. On the other hand, it is known that elongated colloids experience depletion-induced torques close to planar walls, as has been shown analytically and numerically in models of spherocylinders in solvents of hard spheres [54]. These torques depend on both $x_3$ and $\theta$, and they rotate the spherocylinder normal to the wall, i.e., they are contrary to the elastic mechanism. Results in this paper suggest that depletion torques in N-MPCD systems are strong enough to compete with elastic torques. This could be due to the presence of two confining walls and to solvent-solvent correlations [54]. To get a better insight into these mechanisms, an exhaustive numerical analysis could be conducted separately.

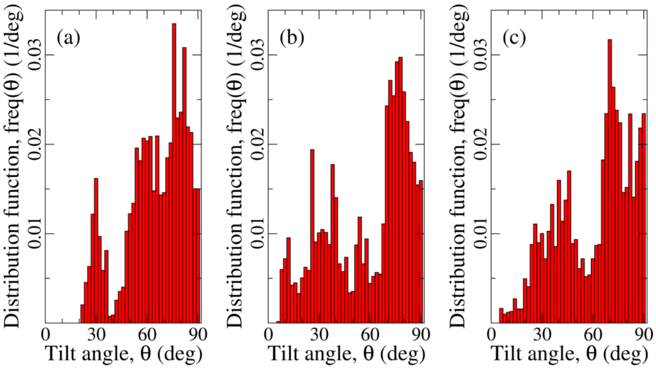

FIG. 5. Relative frequency for the occurrence of tilt angles for spherocylinders immersed in N-MPCD systems with densities: (a) $\bar{N}^c = 20$; (b) $\bar{N}^c = 25$; (c) $\bar{N}^c = 30$. Histograms are constructed using bins of 2° width.

Spherocylinders oscillate around potential minima and dissipate energy. This dynamics can be analyzed in terms of the orientation correlation function [55]

$$\chi(t) = \frac{\langle \cos\alpha(t)\cos\alpha(0)\rangle - \langle\cos\alpha\rangle^2}{\langle\cos^2\alpha\rangle - \langle\cos\alpha\rangle^2}, \tag{14}$$

where $\alpha = \theta - 90^\circ$, and brackets, $\langle\cdots\rangle$, indicate average over thermal fluctuations. In Appendix D, $\chi(t)$ is calculated from a simplified model that considers $\alpha$ as a stochastic variable in a potential well of strength $\Delta\mathcal{V}$, which yields

$$\chi(t) = \frac{\cosh\left(\frac{k_BT}{2\Delta\mathcal{V}}e^{-2\Delta\mathcal{V}t/\eta_R}\right) - 1}{\cosh\left(\frac{k_BT}{2\Delta\mathcal{V}}\right) - 1}, \tag{15}$$

where $\eta_R$ is a rotational friction.

A comparison between the model and simulations appears in Fig. 6. Details of the calculations are also given in Appendix D. For $\bar{N}^c = 25$ and 30, $\chi(t)$ shows the exponential decay expected from Eq. (15). In these cases, statistical noise is noticeable from $t \simeq 2000\Delta t$. For $\bar{N}^c = 20$, the decay of $\chi(t)$ is more erratic due to the prevalence of statistical noise, even for short times. Longer simulations would reduce the effects of noise and improve the comparison. More importantly, Eq. (15) is obtained from a simple linear model, Eq. (D1), and its agreement with simulations suggests that in complex situations where nonlinear forces on anisotropic colloids could be relevant [56], more sophisticated and well-established theories of statistical mechanics [55] could be used for studying their fluctuating behavior.

### C. Dynamics of defects under shear

Spherocylindrical colloids carrying topological defects in sheared nematics are analyzed in this section. For concreteness, the solvent's density is fixed at $\bar{N}^c = 25$, and only

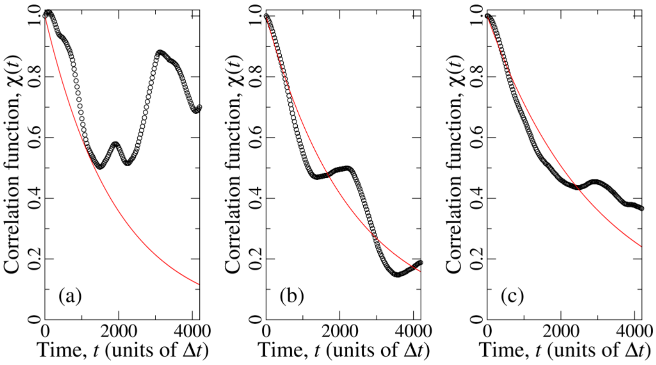

FIG. 6. Autocorrelations of alignment fluctuations of spherocylinders in nematic solvents with densities: (a) $\bar{N}^{\mathrm{c}} = 20$; (b) $\bar{N}^{\mathrm{c}} = 25$; (c) $\bar{N}^{\mathrm{c}} = 30$. Symbols correspond to simulation results. Continuous curves are estimations from a simplified linear model of libration around a potential minimum leading to Eq. (15).

tumbling behavior of the solvent is considered by restricting $\lambda$ to the values 0.25, 0.50, and 0.75. Respectively, Eq. (9) and measurements of $S$ and $S_4$ yield $\lambda' = 0.234$, 0.469, and 0.715. The simulation box is cubic with $V = (40a)^3$, and the solvent is initially oriented along $\hat{\mathbf{e}}_3$. Lees-Edwards boundary conditions are applied considering three different shear rates $\dot{\gamma} = 0.005$, 0.010, and 0.020 $(\Delta t)^{-1}$. These conditions induce tumbling of the nematic fluid in the $\hat{\mathbf{e}}_1$-$\hat{\mathbf{e}}_3$ plane. Single spherocylinders with $L = 12a$ are immersed in these nonequilibrium environments. They are initialized parallel to $\hat{\mathbf{e}}_3$ and in the center of the simulation box. Spherocylinders are driven by shear and also perform tumbling motion because their tumbling parameter is approximately $\lambda_{\mathrm{col}} \simeq 0.6 < 1$, as can be estimated from the expression valid for ellipsoidal particles [42], $\lambda_{\mathrm{col}} = (\zeta^2 - 1)/(\zeta^2 + 1)$.

Spherocylinders exhibit fluctuations that take them out of the $\hat{\mathbf{e}}_1$-$\hat{\mathbf{e}}_3$ plane. Due to their interaction with $\hat{\mathbf{n}}$ and the finite size of the system, this causes a systematic deviation of the global orientation of the solvent, $\hat{\mathbf{n}}_0(t)$, from that plane. To address this problem, pseudonematogens are rotated globally to keep $\hat{\mathbf{n}}_0(t)$ within the tumbling plane. This global rotation is applied after every N-MPCD collision step.

After a short time, a chairlike defect is formed around the colloid. Angle $\theta_{\mathrm{r}}(t) = \cos^{-1}[\hat{\mathbf{e}}'_3(t) \cdot \hat{\mathbf{n}}_0(t)]$ can be used to describe the dynamics of the colloid-defect pair, and defect changes are identified by inspecting the elastic energy $F(\theta_{\mathrm{r}}(t))$. Time series of $F$ are recorded for simulations lasting $2 \times 10^6$ MD-N-MPCD steps. As expected, $F$ is minimum when $\theta_{\mathrm{r}} = 90^\circ$. Hereafter, results are discussed in terms of the normalized energy $\Delta\bar{F} = [F - F(\theta_{\mathrm{r}} = 90^\circ)]/F(\theta_{\mathrm{r}} = 90^\circ)$. Figure 7 presents the results for $\Delta\bar{F}(t)$ and $\theta_{\mathrm{r}}(t)/180^\circ$. Notice that as the colloid rotates, shear maintains oscillations of $\theta_{\mathrm{r}}$. Consequently, $\Delta\bar{F}$ has oscillatory changes of different intensity. Most of these changes are small and correspond to an energy increment caused by the deviation of $\theta_{\mathrm{r}}$ from 90°. However, large gains occur when $\theta_{\mathrm{r}} = 0^\circ, 180^\circ$. These are more frequent and intense for larger $\dot{\gamma}$.

High $\Delta\bar{F}$ peaks are associated with a morphological transformation of the defects. This is observed in Fig. 8, which shows a series of defects for $\lambda = 0.25$ and $\dot{\gamma} = 0.02\,(\Delta t)^{-1}$ during $t \in [17\,400, 17\,950]\Delta t$. When the system crosses the state $\hat{\mathbf{e}}'_3 \parallel \hat{\mathbf{n}}_0$, the defect changes from chairlike to an asymmetric coat and then to chairlike again. The large energy cost for the transformation is paid by the applied shear. For the used parameters, the energy increase could be as large as

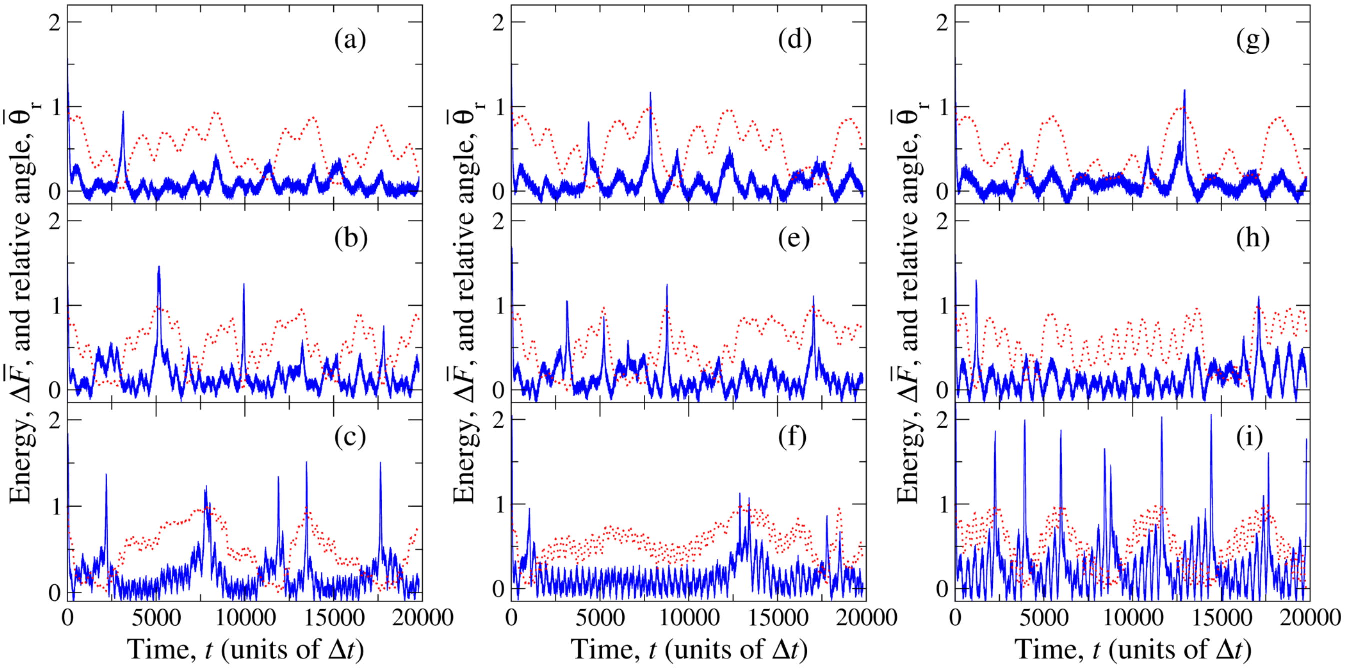

FIG. 7. Elastic energy for spherocylindrical colloids in sheared nematics (continuous curves). Normalized orientation angle of the spherocylinders with respect to $\hat{\mathbf{n}}_0$, $\bar{\theta}_{\mathrm{r}} = \theta_{\mathrm{r}}/180^\circ$ (dotted curves). Parts (a), (b), and (c) correspond to $\lambda = 0.25$ and $\dot{\gamma} = 0.005$, 0.010, and 0.020 $(\Delta t)^{-1}$, respectively; (d), (e), and (f) correspond to $\lambda = 0.50$ and the same order for $\dot{\gamma}$; and (g), (h), and (i) correspond to $\lambda = 0.75$ also with the same order for $\dot{\gamma}$.

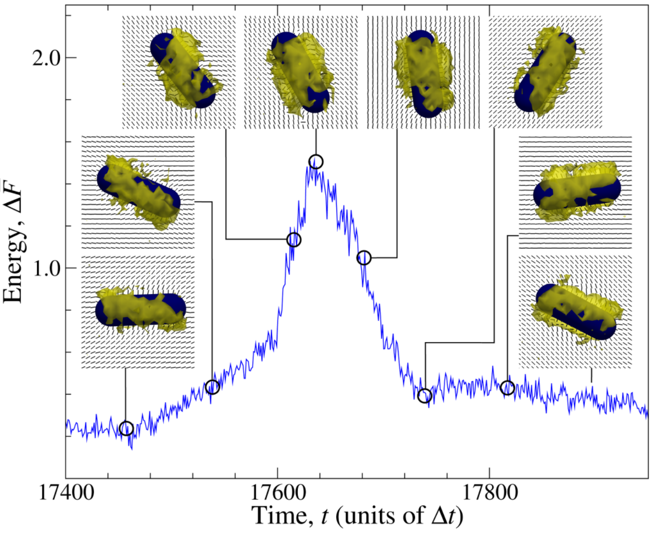

FIG. 8. Morphological changes of the defect around a rotating spherocylinder in a tumbling nematic. The free energy graph is an inset of Fig. 7 for the case $\lambda = 0.25$, and $\dot\gamma = 0.02\,(\Delta t)^{-1}$.

twice the energy of the equilibrium configuration. The initial and final states in the insets of Fig. 8 are minimum energy structure defects connected by a transition pathway of high-energy nonequilibrium states. The state of maximum energy, as mentioned, resembles a coat-type defect that in equilibrium conditions is energetically prohibitive for colloids of the size simulated in this section. Then, it can be interpreted as an unstable dynamic state induced by shear. For confined nematic systems [57], a systematic analysis of the energy landscape shows that minimum free-energy states can be connected by multiple transition pathways with different energy cost. Here, the main result is to show that similar transitions can be promoted by nonequilibrium agents, although no attempt was made to explore the space of all the possible pathways.

Defect changes are due to a hydrodynamic torque on $\hat{\mathbf{n}}$ exerted by the distorted flow around the spherocylinder, $\boldsymbol{\Gamma} = \lambda\hat{\mathbf{n}} \times (\mathbb{D}^c \cdot \hat{\mathbf{n}})$ [58]. To calculate $\boldsymbol{\Gamma}$ in cases in which defect modifications are stronger, configuration $\hat{\mathbf{e}}_3' \parallel \hat{\mathbf{n}}_0$ is considered as depicted in Fig. 9(a), where $\hat{\mathbf{n}}_0$ is signaled and arrows representing the flow field, $\mathbf{v}^c$, are pictured on the plane perpendicular to $\hat{\mathbf{e}}_3$. Notice that in Fig. 9(a), $\theta$ represents the tilt angle of the spherocylinder with respect to the laboratory frame. For simplicity, the calculation is restricted to regions close to the perpendicular symmetry plane of the spherocylinder. There, $\mathbf{v}^c$ surrounds the colloid and has $\hat{\mathbf{e}}_1$ and $\hat{\mathbf{e}}_2$ components that change with $x_1$, $x_2$, and $x_3$. Thus,

$$\mathbb{D}^c = \frac{1}{2}\begin{pmatrix} 2\frac{\partial v_1^c}{\partial x_1} & \frac{\partial v_1^c}{\partial x_2}+\frac{\partial v_2^c}{\partial x_1} & \dot\gamma \\ \frac{\partial v_1^c}{\partial x_2}+\frac{\partial v_2^c}{\partial x_1} & 2\frac{\partial v_2^c}{\partial x_2} & \frac{\partial v_2^c}{\partial x_3} \\ \dot\gamma & \frac{\partial v_2^c}{\partial x_3} & 0 \end{pmatrix}. \qquad (16)$$

In addition, it is assumed that the $\hat{\mathbf{e}}_3'$ axis remains on the $\hat{\mathbf{e}}_1$-$\hat{\mathbf{e}}_3$ plane. The director field is explored for regions intermediately far from the colloid's surface where deviations of $\hat{\mathbf{n}}$ from $\hat{\mathbf{n}}_0$ are small. Then, by using Eq. (16) to calculate $\boldsymbol{\Gamma}$, transforming the result to the $\{\hat{\mathbf{e}}_1', \hat{\mathbf{e}}_3'\}$ system, and retaining only leading contributions in $\hat{\mathbf{n}} \cdot \hat{\mathbf{e}}_3' \gg \hat{\mathbf{n}} \cdot \hat{\mathbf{e}}_1'$, it is found that

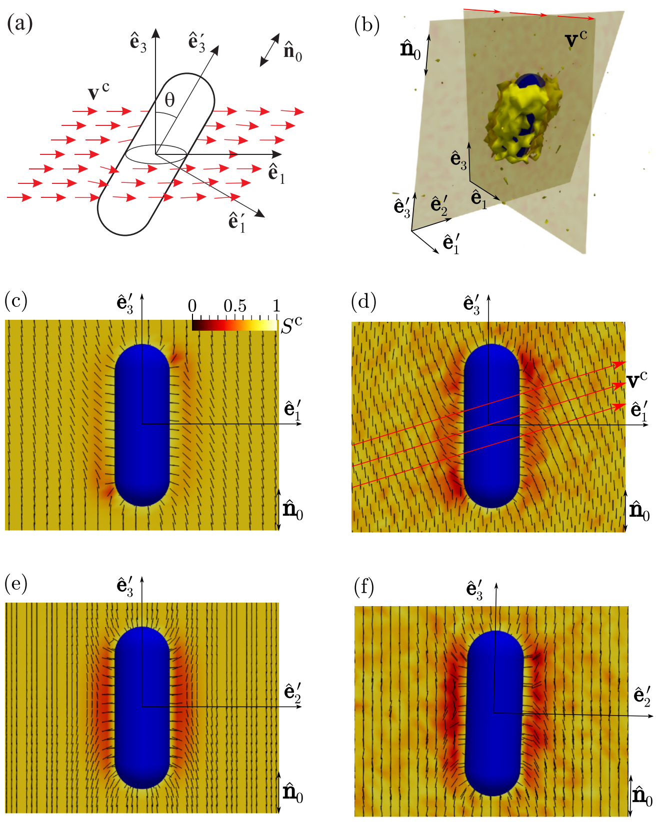

FIG. 9. Changes of the orientation field induced by flow around the spherocylinder. (a) Analyzed model with $\hat{\mathbf{e}}_3' \parallel \hat{\mathbf{n}}_0$. (b) Simulation configuration showing an extended defect and two cutting planes. (c),(d) Director field in the plane $\hat{\mathbf{e}}_1'$-$\hat{\mathbf{e}}_3'$, for equilibrium and nonequilibrium situations, respectively. Streamlines in (d) are indicated through the central portion of the spherocylinder. (e),(f) Same as in (c) and (d), respectively, for the cutting plane $\hat{\mathbf{e}}_2'$-$\hat{\mathbf{e}}_3'$.

$$\boldsymbol{\Gamma} = \frac{1}{2}\lambda\left[\dot\gamma\cos 2\theta + \frac{\partial v_1^c}{\partial x_1}\sin 2\theta\right]\hat{\mathbf{e}}_2' + \frac{1}{2}\lambda\left[\left(\frac{\partial v_1^c}{\partial x_2} + \frac{\partial v_2^c}{\partial x_1}\right)\sin\theta - \frac{\partial v_2^c}{\partial x_3}\cos\theta\right]\hat{\mathbf{e}}_1'. \qquad (17)$$

In Eq. (17) the term proportional to $\dot\gamma$ is the torque on $\hat{\mathbf{n}}$ exerted by the uniform shear, whereas all other terms arise from the distortion of the flow due to the colloidal obstacle. Accordingly, the angular dynamics of $\hat{\mathbf{n}}$ in the bulk and close to the spherocylinder is different. The size of the defect is increased since at close distances from the colloid $\hat{\mathbf{n}}$ does not tumble as $\hat{\mathbf{n}}_0$. Figure 9(b) presents an actual configuration taken from simulation with $\lambda = 0.50$ and $\dot\gamma = 0.20\,(\Delta t)^{-1}$ that satisfies the condition leading to Eq. (17), namely $\hat{\mathbf{e}}_3' \simeq \hat{\mathbf{n}}_0$. Configuration in Fig. 9(b) occurred for $\theta \simeq 19.17^\circ$ at $t = 12\,870\,\Delta t$. Two symmetry planes in the reference frame of the immersed particle, $\hat{\mathbf{e}}_1'$-$\hat{\mathbf{e}}_3'$ and $\hat{\mathbf{e}}_2'$-$\hat{\mathbf{e}}_3'$, are used to analyze distortions by comparing the director field under shear, Figs. 9(d) and 9(f), and in chairlike equilibrium defects, Figs. 9(c) and 9(e). In the nonequilibrium case, the far flow field is parallel to the $\hat{\mathbf{e}}_1'$-$\hat{\mathbf{e}}_3'$ plane, as suggested by the streamlines in Fig. 9(d). By contrasting Figs. 9(c) and

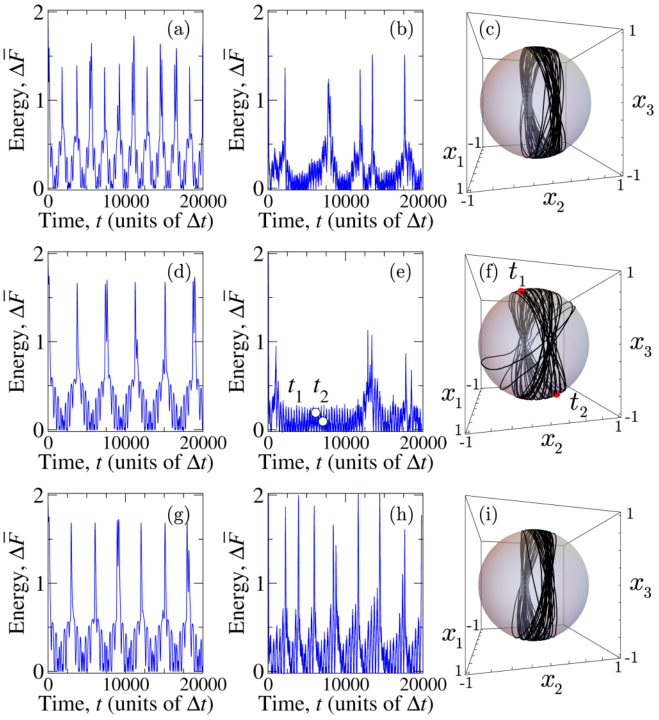

FIG. 10. Energy increments for rotating spherocylinders in nematic fluids sheared at a rate $\dot{\gamma} = 0.020(\Delta t)^{-1}$ for (a),(b) $\lambda = 0.25$; (d),(e) $\lambda = 0.50$; and (g),(h) $\lambda = 0.75$. Parts (a), (d), and (g) are obtained from the approximated model of increments activated close to the state $\theta_r = 0, \pi$. Parts (b), (e), and (h) are simulation results. Parts (c), (f), and (i) represent the trajectories of the long spherocylindrical axis for $\lambda = 0.25$, 0.50, and 0.75, respectively.

9(d), a retardation between $\hat{\mathbf{n}}$ and $\hat{\mathbf{n}}_0$ can be observed in the nonequilibrium situation along the stream lines. This can be attributable to the gradient $\partial v_1^c/\partial x_1$ in Eq. (17) that opposes the effect of $\dot{\gamma}$ when $\mathbf{v}^c$ faces an obstacle along the main stream. The specific contribution of this gradient depends on the slip conditions on the spherocylinder's surface. For the MD-N-MPCD method applied in this work, slip boundary conditions and flow extending behind the colloid are expected [30]. Then, the difference between the orientation patterns in equilibrium and nonequilibrium could be anticipated to reach relatively far distances from the spherocylinder. In turn, flow effects on the $\hat{\mathbf{e}}_2'$-$\hat{\mathbf{e}}_3'$ plane have a shorter range, as observed when equilibrium and nonequilibrium states are compared; see Figs. 9(e) and 9(f), respectively. In this case, flow reorients $\hat{\mathbf{n}}$ toward $\hat{\mathbf{e}}_3'$ mainly in regions near the colloid's surface. This reorientation increases the width of the defect as indicated by the color map for $S^c$ in Figs. 9(c)–9(f). According to Eq. (17), this is due to deviations of flow from simple shear that make $\partial v_1^c/\partial x_2, \partial v_2^c/\partial x_1, \partial v_2^c/\partial x_3 \neq 0$.

The behavior of $\Delta\bar{F}$ under shear can be mimicked by assuming that the solute and solvent tumble independently and that, during tumbling, $\Delta\bar{F}$ follows the equilibrium value at $\theta_r(t)$ exhibiting sudden increments within a narrow range, $\pm\Delta\theta_r$, around $\theta_r = 0^\circ$ and $180^\circ$. This model is elaborated on in Appendix E, and its results are summarized in Fig. 10, where they are compared with simulations for the cases with highest shear rate, $\dot{\gamma} = 0.020\,(\Delta t)^{-1}$.

Despite the many assumptions, a good qualitative agreement can be observed between the simplified model [Figs. 10(a), 10(d) and 10(g)] and simulations [Figs. 10(b), 10(e) and 10(h)]. Such agreement is good in the sense that energy peaks are predicted to be more frequent for $\lambda = 0.25$ and 0.75 [Figs. 10(a), 10(b) 10(g), and 10(h)] than for $\lambda = 0.50$ [Figs. 10(d) and 10(e)]. In addition, for the two former cases, the magnitude of the modeled energy increments is very similar to those observed in simulations. In particular, for $\lambda = 0.75$, all the energy peaks predicted by the model seem to be reproduced by simulations [Figs. 10(g) and 10(h)]. In contrast, in cases $\lambda = 0.25$ and 0.50, some energy peaks are missed or are smaller than expected. This is explained by observing the trajectories of $\hat{\mathbf{e}}_3'$ over the unit sphere and noticing that it abandons the $\hat{\mathbf{e}}_1$-$\hat{\mathbf{e}}_3$ plane [Figs. 10(c), 10(f) and 10(i)]. By doing this, the system avoids the formation of large defects, and $F$ remains small. This is more notorious in the case $\lambda = 0.50$ [Fig. 10(e)], where $\lambda$ and $\lambda_{\text{col}}$ are more similar. It could be expected that in this situation, the spherocylinder has more time to relax toward equilibrium configurations, and deviations of $\hat{\mathbf{e}}_3'$ from the $\hat{\mathbf{e}}_1$-$\hat{\mathbf{e}}_3$ plane could be larger. In simulations, for $t \in (4000, 10\,000)\,\Delta t$, one energy peak could be expected that does not appear because the component of $\hat{\mathbf{e}}_3'$ along $\hat{\mathbf{e}}_2$ is large. In Fig. 10(e), two energy states within this range have been signaled by small circles at times $t_1$ and $t_2$. The corresponding orientations are shown in Fig. 10(f), and they clearly deviate from the shear plane. When these deviations are smaller, large energy changes are more frequent.

To characterize the flow at which the discussed effects could be observed, two dimensionless quantities are considered: (i) the rotational Reynolds number [59], $\text{Re}^{(r)} = (\rho\omega_s l_s^2)/\eta$, where $\rho$ is the mass density of the solvent, $\omega_s$ is the angular velocity, and $l_s$ is a characteristic length; and (ii) the Ericksen number, $\text{Er} = (\gamma_1 v_s l_s)/K$, where $\gamma_1$ is a rotational viscosity and $v_s$ is a typical velocity of the problem. $\text{Re}^{(r)}$ is estimated using $l_s = L$ and $\omega_s = 2\pi/P_{\text{col}}$, where $P_{\text{col}}$ is the colloidal tumbling period. Measurements yield $\text{Re}^{(r)} = 0.14$, 0.35, and 0.88 for $\dot{\gamma} = 0.005$, 0.01, and $0.02\,(\Delta t)^{-1}$, respectively. Since $\text{Re}^{(r)} < 1$, rotation of the spherocylinder is considered to be consistent with linear hydrodynamics [59]. In estimating Er, $l_s = L$ and $v_s = \dot{\gamma}L$ are considered. The ratio $K/\gamma_1$ can be calculated from the decay of the director correlation functions [53,60]. This yields $K/\gamma_1 \simeq 0.62\,a^2(\Delta t)^{-1}$ for nematic fluids simulated with the same parameters as those used throughout this section. Therefore, simulations with $\dot{\gamma} = 0.005$, 0.01, and $0.02\,\Delta t$ have $\text{Er} = 1.16$, 2.32, and 4.65, respectively, indicating that the effects discussed here could be observed when forces induced by flow are similar to or stronger than elastic forces.

It must be remarked that Er depends on the chosen characteristic scales. For instance, in studying defects under Poiseuille flow around spherical colloids [31], instead of using the particle size, $l_s$ was chosen to be the size of the confinement cell.

## IV. CONCLUSIONS

Defects created by individual spherocylindrical colloids in a nematic solvent were studied using the mesoscopic approach of MPCD. The method is based on a MD integrator that takes into account the solvent-colloid interaction and multiparticle collisions that generate nematohydrodynamic behavior at large time and length scales. It was adapted to diverse special cases, namely spherocylinders with fixed orientation in an equilibrium host, colloids performing Brownian motion in a nematic in thermal equilibrium, and colloids that tumble in a nematic driven from equilibrium by a uniform shear. Defects around colloids with fixed orientation were found to be size-dependent. Small spherocylinders (length $\sim 60$ nm) are surrounded by coat-type defects when their orientation coincides with the bulk director field, and by Saturn rings along their largest diameter when orientation is perpendicular. In the parallel setup, defects for spherocylinders of intermediate size (length $\sim 120$ nm) adopt the form of a Saturn ring located close to one of their ends or, alternatively, a metastable chairlike shape extending from one end to the other. This latter is not observed in the parallel arrangement for larger particles (length $\sim 160$ nm). These results are in good agreement with previous studies of similar systems [4,16,18] and indicate that MPCD could be convenient for simulating defects in liquid crystals created by colloids with complex geometry.

When spherocylinders are affected by thermal noise or flow, MD-N-MPCD dealt effectively with their moving boundaries due to its particle-based character. In equilibrium, spherocylinders with intermediate size described a distribution centered in configurations of low elastic energy, although for the used simulation parameters, rather large orientation fluctuations were observed. This coincided qualitatively with observations of ensemble distributions of particles with a similar size and aspect ratio but a different shape [14,17,35]. The information provided by orientation distributions is useful in the problem of tuning interactions between anisotropic colloids leading to novel complex self-assembled structures [18]. More precisely, interactions and defect structures formed around systems of two or more elongated particles in a nematic solvent are functions of the relative orientation and the interparticle distance [4]. Therefore, knowledge of the orientational distribution and its dependence on the system's elasticity could be used to control the probability of occurrence of different orientations and entangled structures. These structures have potential applications such as in displays, materials processing, and fabrication of magnetic responsive materials [12,14].

A linearized model was proposed to describe the relaxation of colloidal orientation fluctuations. Results suggest that this relaxation process could be very slow and that much longer simulations than those conducted here are required to make an exhaustive analysis of this phenomenon. This is a computationally demanding task that goes beyond the scope of the present study.

Nonequilibrium dynamics due to a shearing solvent was analyzed. Simulations were restricted to tumbling nematic phases. Because of the nonuniform flow, the spherocylinder also tumbled with a period dictated by its aspect ratio. This mutual flow-sustained rotation of solvent and solute produced significant changes in the defects that varied from chairlike to a form resembling the coat-type structures that had appeared only for colloids of smaller size. A calculation of the hydrodynamic torque on the director field showed that the aforementioned transformations are produced by the distortion of the streamlines caused by the colloid obstacle. This relation was only indicated generally, Eq. (17), since the precise coefficients will depend on the detailed form of the flow around the spherocylinder, which in turn will change with the slip conditions on its surface. Nevertheless, inspection of director patterns in nonequilibrium states exhibited the effects of torques acting in the direction indicated by the general model. Distortions caused by shear flow have a noticeable increment of elastic energy that could be as large as twice the minimum elastic equilibrium energy. Maximum changes are produced when the rotating director field and the spherocylinder's axis become parallel. When the tumbling periods of the solvent and solute are similar, large energy changes can be evaded by a torsion of the spherocylinder that takes it out from the rotating plane of the director field. However, large energy increments were observed in every simulation of the numerical setup, which was restricted to the regime of small rotational Reynolds numbers, $\mathrm{Re}^{(r)} \sim 10^{-1}$, and Ericksen numbers, $\mathrm{Er} \sim 1$. This suggests that the nonequilibrium dynamic interplay of flow and structure of topological defects presented here could be observable. Besides, dynamical states can be promisingly reproduced on the basis of MD-N-MPCD. This allows us to conjecture that probability distributions of nonequilibrium states could be explored and that the most probable nonequilibrium states and paths toward equilibrium could be identified.

Although to the best of my knowledge there is not an experimental counterpart of the nonequilibrium situation discussed here, in some recent experiments anisotropic colloids with companion defects are moved along controlled paths in liquid crystals close to boundary walls [56]. Further development of the MD-N-MPCD algorithm could be useful in modeling the dynamics of a similar nonequilibrium process that involves colloids under external forces in relative motion with respect to the nematic background.

The numerical method presented here has general advantages and limitations with respect to the existing methods for simulating nematic colloids that are similar to the advantages and limitations that MPCD has in simulating colloids in simple fluids. This problem is interesting in the context of developing algorithms with multiscale character. N-MPCD incorporates hydrodynamics, which is prohibitive for MD methods. It also incorporates fluctuations, which are hard to include in methods based on the continuum formalism. In addition, N-MPCD is simple and very efficient since cell-based operations are very well suited for parallel computing environments. However, further efforts must be conducted to establish a more precise correspondence of multiparticle collision parameters with physical parameters of actual systems.

## ACKNOWLEDGMENTS

This research was funded by CONACyT-Mexico under Grant No. CB2017-2018 A1-S-46608 "Simulación multiescala de cristales líquidos nemáticos" and by La Salle University Mexico under Grants No. NEC-08/18 and No. NEC-13/19.

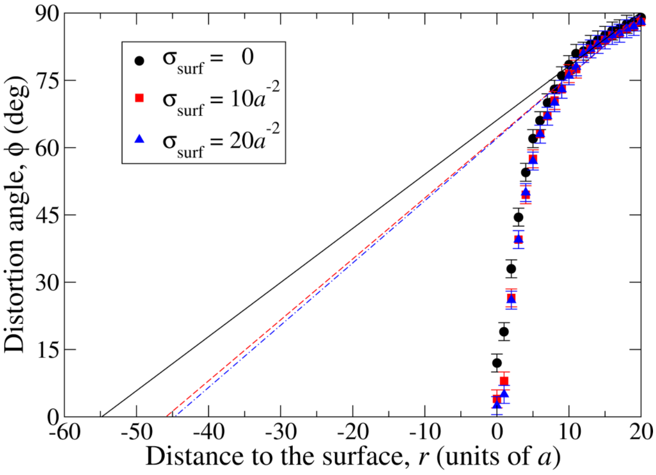

FIG. 11. Estimation of the surface extrapolation length as a function of the surface density of virtual particles on the spherocylindrical colloids.

## APPENDIX A: COMPLETE SET OF SIMULATION PARAMETERS

Throughout this paper, results were obtained using $\Delta t_{\mathrm{MD}} = 10^{-2}\Delta t$, $\chi_{\mathrm{HI}} = 1$, and $\gamma_{\mathrm{R}} = 0.01\, k_{\mathrm{B}}T\, \Delta t$. The solvent-solute interaction was mediated by parameters $\epsilon = 2.5\, k_{\mathrm{B}}T$ and $p = 4$, which are similar to those in MPCD simulations of colloids in isotropic solvents [61]. Results in Secs. III A and III B are obtained with $\lambda = 0.5$. Anchoring conditions on the spherocylinders are controlled by the number density of virtual pseudonematogens on their surfaces, $\sigma_{\mathrm{surf}}$. For small $\sigma_{\mathrm{surf}}$, defects are located close to the spherocylinder and have a diffuse appearance. For large $\sigma_{\mathrm{surf}}$, homeotropic orientation is stronger, defects separate from the colloids, and they can be identified more clearly. This latter case is observed when $\sigma_{\mathrm{surf}} \gtrsim 10a^{-2}$. All results corresponded to $\sigma_{\mathrm{surf}} = 20a^{-2}$. To estimate the anchoring strength, spherocylinders with $L = 16a$ and $\hat{\mathbf{e}}_3' \parallel \hat{\mathbf{e}}_3$ are simulated using $\sigma_{\mathrm{surf}} = 0$, 10, and $20a^{-2}$. Top-ring defects are generated around the colloids. The distortion angle, $\phi$, is defined as the angle between $\hat{\mathbf{n}}^{\mathrm{c}}$ and the normal direction to the spherocylinder's surface. This is measured over the radial direction along the $\hat{\mathbf{e}}_1$ axis on the perpendicular symmetry plane of the spherocylinder. Results are shown in Fig. 11, where $r$ represents the distance to the colloid's surface. At $r = 0$, $\phi$ is 12°, 4°, and 2.5° for $\sigma_{\mathrm{surf}} = 0$, 10, and $20a^{-2}$, respectively. From these values, $\phi$ increases gradually to $\phi = 90^\circ$ at far distances. The surface extrapolation length, $\xi = K/W$, where $W$ is the anchoring energy coefficient, is estimated by a linear fit of the results that permits us to find the distance at which $\phi$ reaches the undistorted value behind the colloid [1]. In the calculation, only the region far from the colloid is considered, where $\phi$ approximates a linear behavior. For $\sigma_{\mathrm{surf}} = 0$, 10, and $20a^{-2}$, respectively, we can obtain $\xi \simeq 54.8$, 45.9, and $44.7a$. The latter can be scaled to $\xi \simeq 450$ nm, which is of the order of magnitude expected for strong anchoring conditions ($\xi \simeq 100$ nm and $W \simeq 10^{-3}$ J/m$^2$) [1].

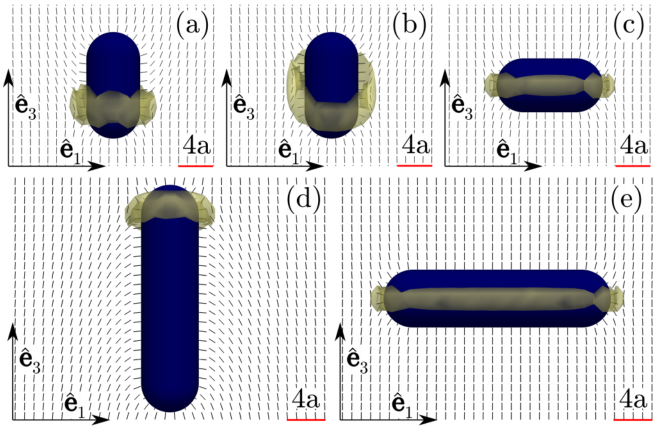

FIG. 12. Defects for spherocylinders with (a)–(c) $\zeta = 1$ and (d),(e) $\zeta = 3$.

## APPENDIX B: CALCULATION OF ELASTIC CONSTANTS

The spatial Fourier transform of $\mathbb{Q}$ is defined by

$$\hat{\mathbb{Q}}(\mathbf{q}) = \frac{V}{2N}\sum_{j=1}^{N}(3\mathbf{u}_j\mathbf{u}_j - \mathbb{I})\exp\{i\,\mathbf{q}\cdot\mathbf{r}_j\}, \tag{B1}$$

where $\mathbf{q}$ is the wave vector, $V$ is the volume, and $i^2 = -1$. For global orientation along $\hat{\mathbf{e}}_3$ and $\mathbf{q} = q_1\hat{\mathbf{e}}_1 + q_3\hat{\mathbf{e}}_3$, one has [62]

$$K_j q_j^2 + K_3 q_3^2 = \frac{9}{4}\frac{S^2 V k_B T}{\langle \hat{Q}_{j3}(\mathbf{q})\hat{Q}_{j3}(-\mathbf{q})\rangle}, \tag{B2}$$

where $j = 1, 2$; and $K_1$, $K_2$, and $K_3$ are the splay, twist, and bend coefficients, respectively. Correlations in Eq. (B2) are calculated in N-MPCD with $V = (40a)^3$, neglecting reorientation by flow [39], and using series of $2 \times 10^5$ data recorded after thermalization. They are adjusted using $K_1$, $K_2$, and $K_3$ as fitting coefficients. For $U = 6.5\, k_{\mathrm{B}}T$ and $\bar{N}^{\mathrm{c}} = 20$, 25, and 30, estimations are $K_1 \simeq K_2 \simeq K_3 = 150.9 \pm 0.3\, k_{\mathrm{B}}T/a$, $187.7 \pm 0.5\, k_{\mathrm{B}}T/a$, and $222.9 \pm 1.3\, k_{\mathrm{B}}T/a$, respectively.

## APPENDIX C: DEFECTS FOR COLLOIDS OF DIFFERENT ASPECT RATIO

Additional simulations of static spherocylindrical colloids with $\sigma = 3a$ and $\zeta = L/2\sigma = 1, 3$ are conducted to show that defect structures reported in Sec. III A are representative for particles with $\zeta \sim 1$. Results are obtained for $\bar{N}^{\mathrm{c}} = 25$. They are shown in Fig. 12. Notice that for parallel alignment and $\zeta = 1$, two structures are found: top-ring [Fig. 12(a)] and chairlike [Fig. 12(b)].

## APPENDIX D: ORIENTATION CORRELATION FUNCTION

Systems simulated in Sec. III B do not exhibit jumps between configurations of minimum energy, $\alpha = 0^\circ, 180^\circ$, during the reported simulation periods. Therefore, a model for libration inside a single potential well can be used. In the simplest case, $\alpha$ follows a two-dimensional linear overdamped dynamics, namely

$$\frac{d\alpha}{dt} = -\frac{2\Delta\mathcal{V}}{\eta_R}\alpha + \frac{1}{\eta_R}\tau(t), \tag{D1}$$

where $\tau(t)$ is a zero-average fluctuating torque satisfying $\langle \tau(t)\tau(0)\rangle = 2\eta_{\rm R} k_{\rm B} T \delta(t)$, with $\delta$ denoting the Dirac delta function [63]. This property and Eq. (D1) permit us to calculate the probability of occurrence of $\alpha$ at time $t$ given that $\alpha = \alpha_0$ at time $t = 0$,

$$W(\alpha, t; \alpha_0) = \frac{1}{\sqrt{\pi \frac{k_{\rm B}T}{\Delta\mathcal{V}}\left(1 - e^{-4\Delta\mathcal{V}t/\eta_{\rm R}}\right)}} \times \exp\left\{-\frac{\left(\alpha - \alpha_0 e^{-2\Delta\mathcal{V}t/\eta_{\rm R}}\right)^2}{\frac{k_{\rm B}T}{\Delta\mathcal{V}}\left(1 - e^{-4\Delta\mathcal{V}t/\eta_{\rm R}}\right)}\right\}, \tag{D2}$$

from which averages on the right-hand side of Eq. (14) can be found yielding Eq. (15).

To compare Eq. (15) with simulations, $\Delta\mathcal{V}$ is estimated from fitting histograms in Fig. 5 with canonical distributions $\propto \exp(\beta \Delta\mathcal{V} \sin^2\theta)\cos\theta$. $\eta_{\rm R}$ is estimated as $\eta_{\rm R} = b\pi\eta(L + 2\sigma)^3/[4 + 3\ln(1 + L/2\sigma)]$, where $b$ is an adjustable parameter and the remaining factor gives the rotational friction of a cylindrical colloid, with $\eta$ the viscosity of the solvent [63]. For N-MPCD, an analytical expression for $\eta$ in terms of the simulation parameters is given in, e.g., Eq. (58) in Ref. [60]. Simulation correlations are measured from the two independent time series used in calculating freq($\theta$) in Fig. 5. Resulting correlations are cut and averaged. Parameter $b$ is adjusted using data for $\bar{N}^{\rm c} = 25$ only, obtaining $b = 0.56 \pm 0.2$ when fitting is restricted to $t \in [0, 4000\Delta t]$. The small deviation $b \neq 1$ could be attributable to the differences in slip conditions and geometric features of the model with respect to those in Ref. [63].

## APPENDIX E: MODEL FOR ELASTIC ENERGY UNDER SHEAR

$\Delta\bar{F}(t)$ is modeled under the assumptions described in Sec. III C. Here, let $\theta_{\rm col}(t) \equiv \theta(t)$ and $\theta_{\rm nem}(t) = \cos^{-1}(\hat{\mathbf{n}}_0 \cdot \hat{\mathbf{e}}_3)$. Tumbling angles for colloid and solvent are approximated by independent Jeffery's orbits [64],

$$\theta_{\rm col,nem}(t) = \arctan\left[P_{\rm col,nem} \tan\left(\frac{\dot{\gamma}t}{P_{\rm col,nem} + \frac{1}{P_{\rm col,nem}}}\right)\right], \tag{E1}$$

where $P_{\rm col} = 2\pi/[\dot{\gamma}\sqrt{1 - \lambda_{\rm col}^2}]$ and $P_{\rm nem} = 2\pi/[\dot{\gamma}\sqrt{1 - \lambda'^2}]$ denote the respective tumbling periods. The equilibrium energy of the system is taken as $A\cos^2\theta_{\rm r}$, where $A \propto F(\theta_{\rm r} = 90^\circ) - F(\theta_{\rm r} = 0^\circ)$ [15]. Here, $A$ is permitted to be time-dependent and to follow a dissipative process toward equilibrium, $A_{\rm eq}$, plus an increasing contribution toward a maximum value associated with the coat-type defect, $A_{\rm coat}$, specifically

$$\frac{dA}{dt} = -\kappa_0(A - A_{\rm eq}) - \kappa_1 \xi(\theta_{\rm r}(t))(A - A_{\rm coat}), \tag{E2}$$

where $\xi(\theta_{\rm r}(t))$ is selected to be significant only when $\theta_{\rm r}(t) \simeq 0$, namely

$$\xi(\theta_{\rm r}) = \frac{\exp[\cos^2\theta_{\rm r}/(\Delta\theta_{\rm r})^2] - 1}{\exp[1/(\Delta\theta_{\rm r})^2] - 1}. \tag{E3}$$

Equations (E2) and (E3) are solved numerically using $\theta_{\rm r} = \theta - \theta_{\rm nem}$ and Eq. (E1). For plots in Fig. 10, $A_{\rm eq} = 0.58$, $A_{\rm coat} = 3.42$, and $\kappa_0 = 0.01\,(\Delta t)^{-1}$ are estimated from relaxation of coat-type to chairlike defects; $\lambda'$ values specified in Sec. III C are used; and $\kappa_1 = 5\kappa_0$ and $\Delta\theta_{\rm r} = 2.5^\circ$ are found to adjust the model with simulations.

---

[1] I. Muševič, *Liquid Crystal Colloids* (Springer, New York, 2017).

[2] I. Muševič, Eur. Phys. J.: Spec. Top. **227**, 2455 (2019).

[3] E. Bukusoglu, M. B. Pantoja, P. C. Mushenheim, X. Wang, and N. L. Abbott, Annu. Rev. Chem. Biomol. Eng. **7**, 163 (2016).

[4] F. R. Hung, O. Guzmán, B. T. Gettelfinger, N. L. Abbott, and J. J. de Pablo, Phys. Rev. E **74**, 011711 (2006).

[5] M. Kleman and O. D. Lavrentovich, *Soft Matter Physics: An Introduction* (Springer, New York, 2003).

[6] D. Henao, A. Majumdar, and A. Pisante, Calc. Var. **56**, 55 (2017).

[7] H. Stark, Phys. Rep. **351**, 387 (2001).

[8] C. Völtz, Y. Maeda, Y. Tabe, and H. Yokoyama, Phys. Rev. Lett. **97**, 227801 (2006).

[9] V. Tomar, T. F. Roberts, N. L. Abbott, J. P. Hernández-Ortiz, and J. J. de Pablo, Langmuir **28**, 6124 (2012).

[10] C. P. Lapointe, T. G. Mason, and I. I. Smalyukh, Science **326**, 1083 (2009).

[11] C. P. Lapointe, K. Mayoral, and T. G. Mason, Soft Matter **9**, 7843 (2013).

[12] M. A. Gharbi, M. Cavallaro Jr., G. Wu, D. A. Beller, R. D. Kamien, S. Yang, and K. J. Stebe, Liq. Cryst. **40**, 1619 (2013).

[13] S. Hashemi, U. Jagodič, M. Mozaffari, M. R. Ejtehadi, I. Muševič, and M. Ravnik, Nat. Commun. **8**, 14026 (2017).

[14] D. K. Sahu, T. G. Anjali, M. G. Basavaraj, J. Aplinc, S. Čopar, and S. Dhara, Sci. Rep. **9**, 81 (2019).

[15] S. V. Burylov and Y. L. Raikher, Phys. Rev. E **50**, 358 (1994).

[16] D. Andrienko, M. P. Allen, G. Skačej, and S. Žumer, Phys. Rev. E **65**, 041702 (2002).

[17] U. Tkalec, M. Škarabot, and I. Muševič, Soft Matter **4**, 2402 (2008).

[18] F. R. Hung, Phys. Rev. E **79**, 021705 (2009).

[19] Q. Liu, B. Senyuk, J. Tang, T. Lee, J. Qian, S. He, and I. I. Smalyukh, Phys. Rev. Lett. **109**, 088301 (2012).

[20] M. Tasinkevych, F. Mondiot, O. Mondain-Monval, and J.-C. Loudet, Soft Matter **10**, 2047 (2014).

[21] M. Nikkhou, M. Škarabot, S. Čopar, M. Ravnik, S. Žumer, and I. Muševič, Nat. Phys. **11**, 183 (2015).

[22] S. M. Hashemi and M. R. Ejtehadi, Phys. Rev. E **91**, 012503 (2015).

[23] S. P. Yadav and S. Singh, Prog. Mater. Sci. **80**, 38 (2016).

[24] M. Nikkhou and I. Muševič, Soft Matter **14**, 9819 (2018).
[25] S. Khullar, C. Zhou, and J. J. Feng, Phys. Rev. Lett. **99**, 237802 (2007).
[26] C. Zhou, P. Yue, and J. J. Feng, J. Fluid Mech. **593**, 385 (2007).
[27] Y. Luo, D. A. Beller, G. Boniello, F. Serra, and K. J. Stebe, Nat. Commun. **9**, 3841 (2018).
[28] M. Yoneya, J.-I. Fukuda, H. Yokoyama, and H. Stark, Mol. Cryst. Liq. Cryst. **435**, 75 (2005).
[29] T. Araki and H. Tanaka, J. Phys.: Condens. Matter **18**, L193 (2006).
[30] D. Reyes-Arango, J. Quintana-H., J. C. Armas-Pérez, and H. Híjar, Physica A **547**, 123862 (2020).
[31] T. Stieger, M. Schoen, and M. G. Mazza, J. Chem. Phys. **14**, 054905 (2014).
[32] T. Stieger, S. Püschel-Schlotthauer, M. Schoen, and M. G. Mazza, Mol. Phys. **114**, 259 (2016).
[33] A. Sengupta, Liq. Cryst. Today **24**, 70 (2015).
[34] S. Mondal, A. Majumdar, and I. M. Griffiths, J. Colloid Interface Sci. **528**, 431 (2018).
[35] A. Eremin, P. Hirankittiwong, N. Chattham, H. Nádasi, R. Stannarius, J. Limtrakul, O. Haba, K. Yonetake, and H. Takezoe, Proc. Natl. Acad. Sci. (USA) **112**, 1716 (2015).
[36] D. J. Earl, J. Ilnytskyi, and M. R. Wilson, Mol. Phys. **99**, 1719 (2001).
[37] D. Frenkel and B. Smit, *Understanding Molecular Simulation* (Academic, London, 2002).
[38] I. P. Omelyan, Comput. Phys. Commun. **109**, 171 (1998).
[39] T. N. Shendruk and J. M. Yeomans, Soft Matter **11**, 5101 (2015).
[40] T. Ihle and D. M. Kroll, Phys. Rev. E **63**, 020201(R) (2001).
[41] A. Majumdar, Eur. J. Appl. Math. **21**, 181 (2010).
[42] L. A. Archer and R. G. Larson, J. Chem. Phys. **103**, 3108 (1995).
[43] H. Híjar, D. M. de Hoyos, and I. Santamaria-Holek, J. Chem. Phys. **136**, 114109 (2012).
[44] F. M. Leslie, Arch. Ration. Mech. Anal. **28**, 265 (1968).
[45] G. Gompper, T. Ihle, D. M. Kroll, and R. G. Winkler, in *Advanced Computer Simulation Approaches for Soft Matter Sciences III*, edited by C. Holm and K. Kremer (Springer, Berlin, 2009), Vol. 221, pp. 1–87.
[46] K.-W. Lee and M. G. Mazza, J. Chem. Phys. **142**, 164110 (2015).
[47] S. Mandal and M. G. Mazza, Phys. Rev. E **99**, 063319 (2019).
[48] A. Malevanets and R. Kapral, J. Chem. Phys. **110**, 8605 (1999).
[49] A. Lamura and G. Gompper, Eur. Phys. J. E **9**, 477 (2002).
[50] J. K. Whitmer and E. Luijten, J. Phys.: Condens. Matter **22**, 104106 (2010).
[51] D. S. Bolintineanu, J. B. Lechman, S. J. Plimpton, and G. S. Grest, Phys. Rev. E **86**, 066703 (2012).
[52] A. W. Lees and S. F. Edwards, J. Phys. C **5**, 1921 (1972).
[53] H. Híjar, R. Halver, and G. Sutmann, Fluct. Noise Lett. **18**, 1950011 (2019).
[54] R. Roth, R. van Roij, D. Andrienko, K. R. Mecke, and S. Dietrich, Phys. Rev. Lett. **89**, 088301 (2002).
[55] E. Praestgaard and N. van Kampen, Mol. Phys. **43**, 33 (1981).
[56] Y. Luo, T. Yao, D. A. Beller, F. Serra, and K. J. Stebe, Langmuir **35**, 9274 (2019).
[57] H. Kusumaatmaja and A. Majumdar, Soft Matter **11**, 4809 (2015).
[58] H. Pleiner and H. R. Brand, in *Pattern Formation in Liquid Crystals*, edited by A. Buka and L. Kramer (Springer, New York, 1996), pp. 15–67.
[59] J. Happel and H. Brenner, *Low Reynolds Number Hydrodynamics* (Martinus Nijhoff, Hague, 1983).
[60] H. Híjar, Condens. Matter Phys. **22**, 13601 (2019).
[61] J. T. Padding and A. A. Louis, Phys. Rev. E **74**, 031402 (2006).
[62] M. P. Allen and D. Frenkel, Phys. Rev. A **37**, 1813 (1988).
[63] J. K. G. Dhont, *An Introduction to Dynamics of Colloids* (Elsevier, Amsterdam, 1996).
[64] G. B. Jeffery, Proc. R. Soc. London A **102**, 161 (1922).